

A Shear Compression Disk Specimen with Controlled Stress Triaxiality Under Dynamic Loading

B. Karp · A. Dorogoy · D. Rittel

Received: 11 September 2011 / Accepted: 18 May 2012 / Published online: 30 May 2012
© Society for Experimental Mechanics 2012

Abstract This paper presents an experimental and numerical study of the potential of the Shear Compression Disk specimen (SCD) to characterize the plastic flow and fracture of metals under various levels of stress triaxiality at strain rates of up to 10^4 1/s. The main loading mode in that specimen is shear with triaxiality ranging from 0 to -0.8. The specimen is relatively small and fits into a standard split Hopkinson pressure bar system. Aluminum 7075-T651 alloy was chosen for a test case study. Experimental and numerical investigations reveal the adequacy of the SCD specimen for the study of mechanical properties of materials under high strain-rates and low, though wide, range of stress triaxialities.

Keywords a. triaxiality · b. ductile fracture · c. flow properties · d. finite elements · e. dynamic loading · f. high strain rate

Introduction

Since the classical experimental studies of Bridgman [1] on the effect of pressure on fracture, followed by the analytical basis for void growth, laid by Rice and Tracey [2], it is well acknowledged that fracture of metals is sensitive to the

triaxiality of the stress prior to and at fracture. It is also accepted that fracture might depend on the strain rate, as well. Therefore, for a reliable experimental characterization of fracture it is desirable to control reasonably well both the triaxiality and the strain rate within the gauge volume. That non-trivial endeavor was expressed clearly by Ramesh [3]: “The development of models for constitutive behavior that can be used for multiaxial stress states is one of the goals of this area of research, but is quite difficult at high strain rates because of the complexity of the experimental techniques involved”. A concise review of experimental methods for high strain rate investigation of materials is given by Edwards [4], emphasizing the dependence of the results on the experimental setup.

Specimens generating various levels of stress triaxiality under high strain rate loading have been suggested in several studies. Some of these specimens are: hat specimens (e.g., [5, 6]), shear compression specimen (SCS) (e.g., [7, 8]), compression specimen enclosed in sleeve (e.g., [9, 10]), butterfly specimen (e.g., [11] for quasi-static loading and [12] for high strain rate), and tension specimen, with or without a notch (e.g., [13–16]). Each specimen has some advantages and limitations. While tensile and butterfly specimens are suitable for high triaxiality levels, most of the other specimens aim to zero triaxiality and less (including butterfly specimen). Yet, the control over triaxiality is relatively limited with a need for several different types of specimens to cover a wide range of triaxialities (e.g., [17]). Although the estimation of triaxiality level in the experiments relies on the numerical evaluation of each specimen, a different set of assumptions is required for each specimen, thus losing the common ground for the whole set of obtained data.

In the present paper a new specimen, the Shear Compression Disc (SCD), is examined for its adequacy for the

B. Karp (✉)
Department of Mechanical Engineering, Ben-Gurion University
of the Negev,
P.O.B. 653, Beer-Sheva 84105, Israel
e-mail: bkarp@bgu.ac.il

A. Dorogoy · D. Rittel
Faculty of Mechanical Engineering, Technion – Israel Institute
of Technology,
32000, Haifa, Israel

investigation of the effect of triaxiality and strain rate on plastic flow and fracture. This study is an extension of the previous investigation addressing quasi-static condition by Dorogoy et al. [18], where the specimen was introduced for the first time. It was demonstrated that the SCD specimen has several advantages over currently available specimens, in particular, a relatively convenient way to control the triaxiality within the gauge, as well as its constant value throughout the complete deformation process up to fracture. Here, experimental and numerical studies of SCD specimens, made of aluminum 7075-T651, were extended to high strain-rate conditions. A Split Hopkinson pressure bar system (SHPB) was used to impose high strain rate within the specimen, preserving the ability to control the stress triaxiality. Such an extension has the advantage of relying on the same set of assumptions over a wide range of strain rates, from quasi-static up to 10^4 1/sec and enabling one to investigate either separate or joint effects of triaxiality and strain rate on fracture phenomena.

Results for 12 specimens exposed to high strain rate conditions at several triaxiality levels are reported. The interpretation of the results concentrates on plastic flow and fracture. The results obtained with the new specimen are compared to those obtained with other commonly accepted specimen geometries (cylinders and SCS). It is found that the SCD specimen yields a reasonably reliable characterization of plasticity and fracture properties at high strain rates, as observed in quasi-static loading conditions [18].

In Section 2 the experimental setup and procedure are described. Experimental details are given in Section 3, while the numerical details are presented in Section 4. The experimental results and their interpretation are detailed in Section 5, followed by a discussion and summary section.

Specimen, Setup, and Procedure

The specimen examined in this study has been described in [18] in the context of a quasi-static loading. The only modification required here is an adapter for positioning the same

specimen in the split Hopkinson pressure bar system, as shown schematically in Fig. 1. That adapter is used both for the unconfined (Fig. 1(a)) and the confined (Fig. 1(b)) configurations. The exact dimensions of the adapter, fitting an existing SHPB system with rod diameter of 12.7 mm, are detailed in Fig. 2.

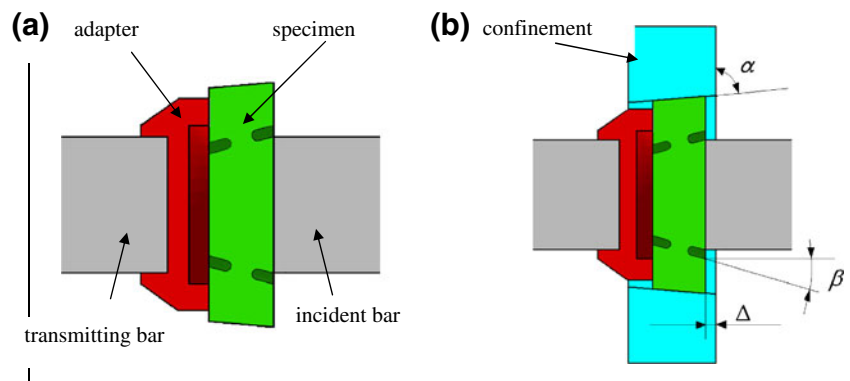
The experimental procedure is identical to the described in [18] for the static examination. Control of the triaxiality level is achieved by predefined insertion of the specimen into the confinement. The target initial and subsequent triaxiality of the stress is achieved by proper selection of the angles α and β , and the insertion distance Δ (shown in Fig. 1(b)). The values of these variables are determined by numerical simulations as described in [18]. The triaxiality (t_r) is defined by $t_r = \frac{\sigma_m}{\sigma_{eq}}$, where the effective pressure is defined by $\sigma_m = \frac{1}{3}\sigma_{ii}$ (positive in tension) and $\hat{\sigma}_{eq}$ is the equivalent von Mises stress.

Except for the optional preceding step of specimen insertion into the confinement, the experimental procedure itself is identical to a standard experiment in SHPB system. No revision of the SHPB system is required. The SHPB standard strain recordings are interpreted to extract flow and fracture properties. Since the specimen undergoes large deformations, the interpretation of the data is based on a hybrid numerical-experimental iterative procedure in which the stress–strain curve is obtained first, followed by determination of the fracture strain (detailed below).

Experiments

A total of 12 tests were conducted up to fracture of the specimen: 7 tests without pre load and 5 tests with pre load. The experimental details which include experiment number, specimen number, tilt angle of the slots, the magnitude of pre load, and the pressure which accelerated the 205 cm steel striker are listed in Table 1. The strain rate is found to lie in the range of 3,000–14,000 1/s. Four variations of specimen geometries were used which differ by the tilt angle

Fig. 1 A section view through the experimental setups. (a). Non confined specimen. (b). Confined specimen. Specimen and experiment parameters α , β and Δ are shown as well



of the slots: $\beta=0^\circ, 10^\circ, 15^\circ$ and 20° , all chosen to cover a wide range of triaxiality levels. The combination of tilt angle and the amount of pre load travel Δ were chosen to fix not only the initial triaxiality level, but also make it almost constant along the whole deformation process. The triaxiality values given in Table 1 are target triaxialities estimated numerically from the quasi-static configuration detailed in [18]. Since material properties are generally rate-dependent, the actual triaxiality level generated within the specimen in the dynamic experiments are re-calculated numerically in the course of the data analysis and given below in Table 2.

Numerical Analysis

Numerical transient axisymmetric analyses were conducted with Abaqus Explicit code [19] to simulate all experiments. The confined and the unconfined configurations were modeled separately, as shown in Fig. 3(a) and (b). For the unconfined specimens the holder is not modeled and only half of the incident bar is included. For the confined specimens the incident bar is not modeled. That omission results in a reduced number of elements without sacrificing the validity of the simulation.

A typical mesh which is shown in figure in Fig. 3(a) consist of 28316 elements and 30482 nodes: 28266 are linear quadrilateral elements of type CAX4R and 50 are linear triangular elements of type CAX3. The size of the elements within the gauge is $\sim 1/20$ of the gauge length. The choice of that element size has been confirmed by convergence verifications. Average field values within the gauge along the active line (designated by a red line in Fig. 3(a)) are extracted from the analysis. The validity of the average values was confirmed by inspection of detailed local values, as reported in [18]. The strain history on the surface of the incident and transmitting bars at the location of the strain gauges in the actual experimental setup is obtained as well.

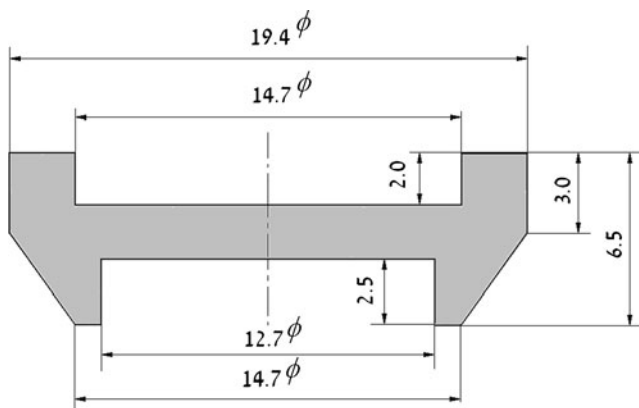


Fig. 2 A detailed sketch of the adapter with nominal dimensions

Table 1 Specimen's data and experimental conditions for the twelve tests

Experiment	Specimen number	β°	Pre load Δ [mm]	Target triaxiality t_r	P[atm]
1	2	20	0.0	$-0.9 < t_r < -0.7$	4.5
2	8	15	0.0	-0.4	3.5
3	17	15	0.0	-0.4	4.0
4	11	10	0.0	-0.2	4.0
5	12	10	0.0	-0.2	3.5
6	14	0	0.0	-0.1	2.9
7	16	0	0.0	-0.1	3.5
8	4	20	0.75	-0.9	6.0
9	6	15	0.5	-0.7	6.0
10	18	15	0.5	-0.7	5.0
11	19	15	0.5	-0.7	5.0
12	20	15	0.75	$-0.9 < t_r < -0.7$	5.0

Frictional “surface to surface” contact was applied between all contacting surfaces. A typical value of $f=0.1$ for Coulomb coefficient of friction between lubricated surfaces was adopted.

The impact on the unconfined specimens was simulated in one step in which the measured experimental stresses were applied to the end of the simulated incident bar. That stress was calculated from the actual strains measured for each experiment (strain gauge location shown in Fig. 3). The loading of the confined specimen was performed in three steps: 1) Pre-load, 2) Release, 3) Impact. In the first step the bottom of the holder is fixed while the specimen, adapter and transmitting bar were displaced “quasi-statically” by an amount of Δ mm. The displacement duration of 2 ms was chosen to diminish inertial effects. The duration of the release step was set to 100 μ s, during which the load is released and the adapter and transmitting bar are put in contact with each other and the specimen. This step serves

Table 2 Triaxiality, strain rate and fracture strains for the tested specimens, including results reported for quasi-static experiments in [18]

specimen	Triaxiality $t_r = -\frac{\sigma_m}{\sigma_{Mises}} ; \sigma_m = \frac{1}{3}\sigma_{ii}$	Strain rate $\left[\frac{1}{s}\right]$	Fracture strain ϵ_p^f
	-0.06	0.0001	0.16
	-0.20	0.0001	0.20
	-0.41	0.0001	0.28
	-0.72	0.0001	0.70
	-0.90	0.0001	1.20
14	0.01	3060	0.07
12	-0.18	3840	0.10
17	-0.34	5524	0.15
19	-0.67	14725	0.35
4	-0.8	11300	0.65

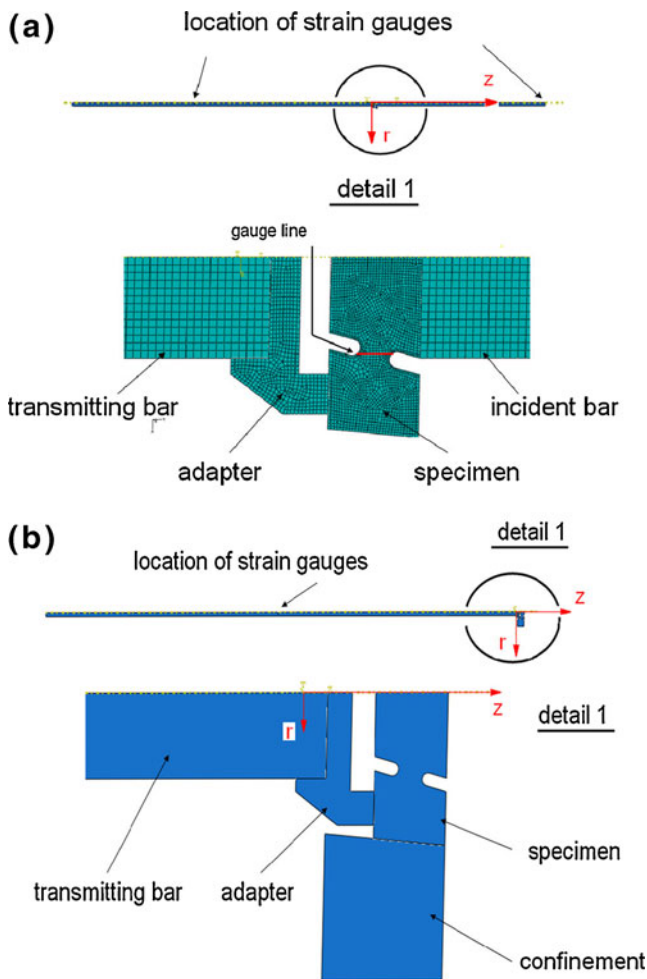
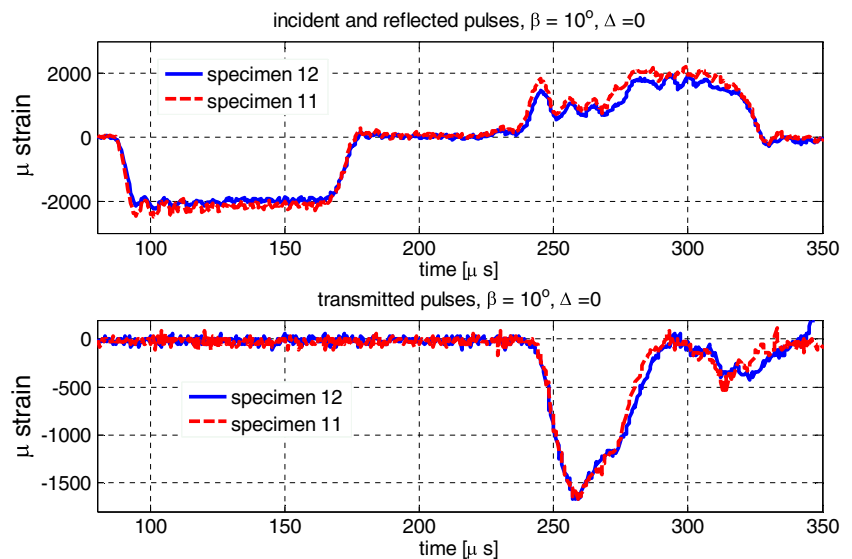


Fig. 3 Numerical models for simulation of experiments. (a). Unconfined specimen. (b). Confined specimen

as a starting condition for the dynamic experiment, determining the initial triaxiality level. In the dynamic (impact)

Fig. 4 Typical experimental results for unconfined specimens with $\beta=10^\circ$



step, the experimentally measured displacement is used as an input to the inner upper surface of the specimen. These displacements are calculated from the measurements of the incident pulse and the reflected pulse by the strain gauges which are located on the mid length of the incident bar.

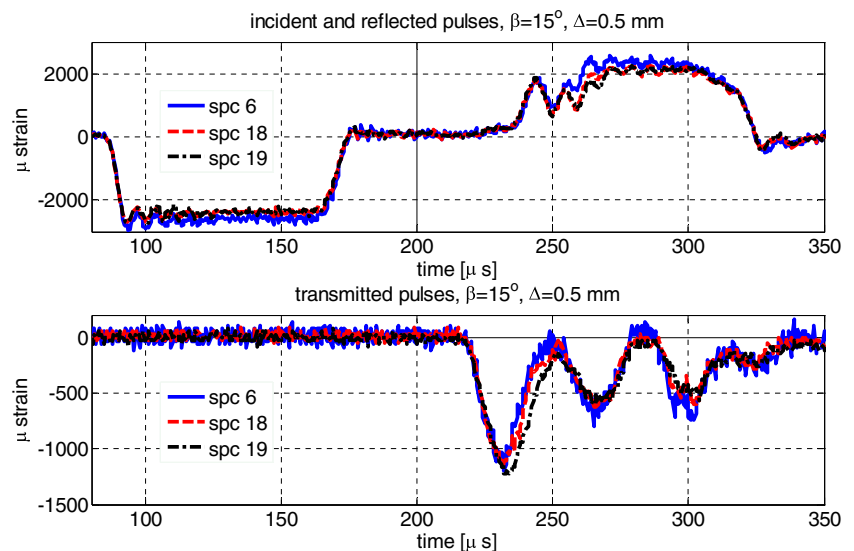
Results

The experimental results consist of the transient recorded strains obtained from the strain gauges which are mounted on the incident and transmitting bars. Analysis of the signals for stress–strain curve is similar to the standard SHPB procedure for compression specimens with some modifications accounting for shear specimens (e.g., [20–25]). Analysis of the data for extraction of fracture strain is developed specifically for that specimen and described in the sequel.

Typical recording of the two types of tests (unconfined and confined) are shown in Figs. 4 and 5, respectively. Figure 4 shows the raw strain signals obtained for two unconfined specimens with $\beta=10^\circ$ (experiments 4 and 5 in Table 1). Figure 5 shows the strain history obtained for three experiments with confined specimens with $\Delta=0.5\text{ mm}$ and $\beta=15^\circ$ (experiments 9, 10 and 11 in Table 1). Good repeatability of the signals is noted, especially taking into account the slightly different velocities of the striker in each experiment (different pressures as detailed in Table 1) as also evident from the slight difference between the incident pulses.

In the following sections the interpretation of the experimental results is detailed. The procedure consists of two consecutive steps: the first one is aimed to obtain the stress–strain curve valid for the particular strain rate. That step is required only if there is a convincing reason to assume that the stress–strain curve of the material examined is sensitive

Fig. 5 Typical experimental results for confined specimens with $\Delta=0.5\text{ mm}$ and $\beta=15^\circ$



to the strain rate. In the second step, the strain at fracture is extracted.

Dynamic Stress–strain Curve

To account for a rate effect on the stress–strain curve, an iterative process was performed to derive the dynamic curve. As a first guess, the quasi-static curve, taken from [18], is used to simulate the experiment. The subsequent stress–strain curves are modified up to conversion to the experimental signal. The criterion for conversion of the iteration process was chosen to be a negligible (in comparison to the typical experimental scatter) difference between the measured transmitted strain (Figs. 4 and 5) and the strains extracted from the simulation.

Simulated transmitted signals for experiments 11 and 12 with four $\sigma - \varepsilon$ curves are shown in Fig. 6, along with the actual experimental recording. For simplicity, the variation of stress–strain curve is limited to four values of yield stress, shown in Fig. 7. It can be observed that for specimen 11 a good agreement with the experimental result is obtained with $\sigma_y=603\text{ MPa}$, while for specimen 12, the curve which correspond to $\sigma_y=643\text{ MPa}$ yields a better fit. Since the numerical simulation does not include fracture at this stage, the departure between the actual signal and the numerical one is evident (and will be discussed in the next section).

Repeating the same procedure for all specimens yielded stress–strain curves bounded by two limiting curves shown in Fig. 7 (designated by the gray shaded area). Figure 7 also shows the quasi-static curve used as an initial guess and one intermediate curve. This completes the iterative process for determination of stress–strain curve at high strain rate loading.

Apparently, the difference between the two dynamic stress–strain curves defining the gray area can be considered as a rough indication of the accuracy of this procedure. Yet,

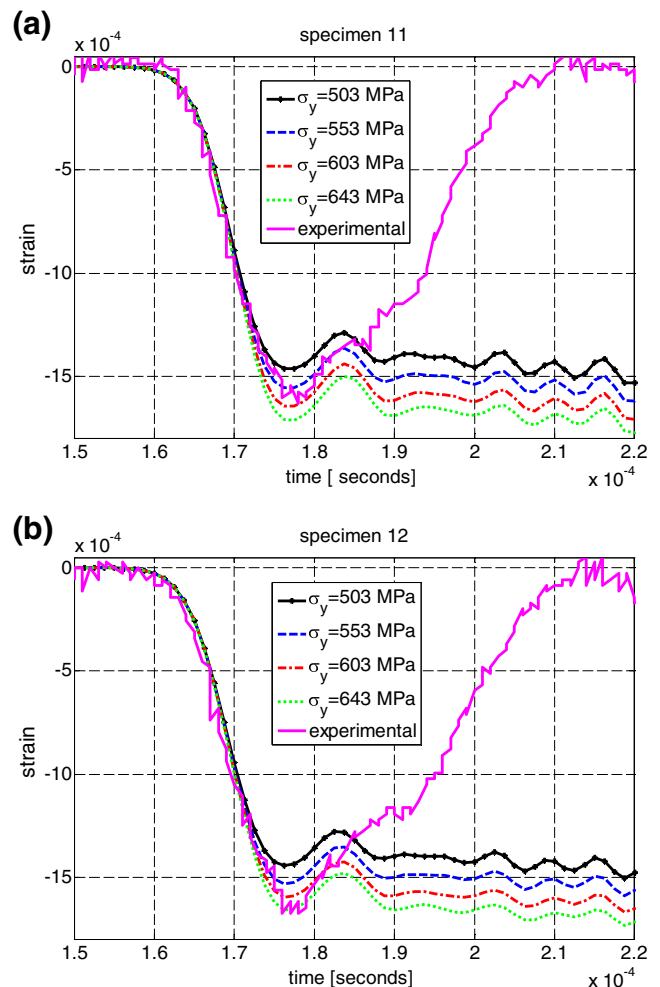


Fig. 6 Comparison of the numerically obtained transmitted pulse due to four $\sigma - \varepsilon$ curves to the experimental pulse. (a). Specimen 11 - agreement with the $\sigma - \varepsilon$ curve which corresponds to $\sigma_y=603\text{ MPa}$. (b). Specimen 12 - agreement with the $\sigma - \varepsilon$ curve which corresponds to $\sigma_y=643\text{ MPa}$

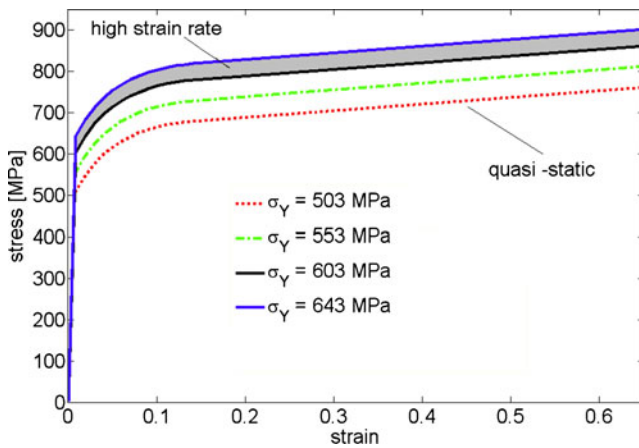


Fig. 7 Quasi-static stress-strain curve ($\sigma_Y=503$ MPa) for aluminum 7075-T651 and the dynamic curve (gray area) obtained for the strain rate $\dot{\varepsilon} \approx 10^4$ 1/s

it is conceivable that finer increments of stress-strain curves iterations, together with strain hardening adjustment, might reduce that scatter. Moreover, due to the small sample size in the present preliminary study, the experiments regarded in Fig. 7 as of single strain rate (of approximately 10^4 1/s) while the actual strain rate lies between 3,000–14,000 1/s.

As an additional confirmation for the accuracy of the obtained stress-strain curve at high strain-rate loading, the experimental results were interpreted directly by a different and independent procedure, resembling in principle the commonly employed procedure to interpret results obtained with compression specimens in a SHPB system. That procedure and its results are detailed in Appendix A. An agreement between both procedures is noticeable.

Fracture Strain

The fracture strain $\varepsilon_p^f(tr, \dot{\varepsilon})$, which is assumed to depend both on the triaxiality (tr) and the strain rate ($\dot{\varepsilon}$), is determined with the aid of a numerical simulation of the experiment. Once the optimal stress-strain curve is determined, it is assumed that the point of departure of the numerical simulation from the experimental raw data (like in Fig. 6) corresponds to fracture.

Let us consider the results obtained with three specimens 19, 11, and 12. The raw strain history and numerical simulation without fracture criterion are shown in Fig. 8 for three experiments (two configurations). Similar simulations have been performed with the failure criterion available in Abaqus code, referred to as “ductile failure” [26]. That criterion removes elements which have reached a pre-defined value of equivalent plastic strain, irrespective of the level of triaxiality or strain rate. Different values of fracture strain were simulated while using the same dynamic $\sigma - \varepsilon$ curve obtained in the previous section. The resulting strain pulse

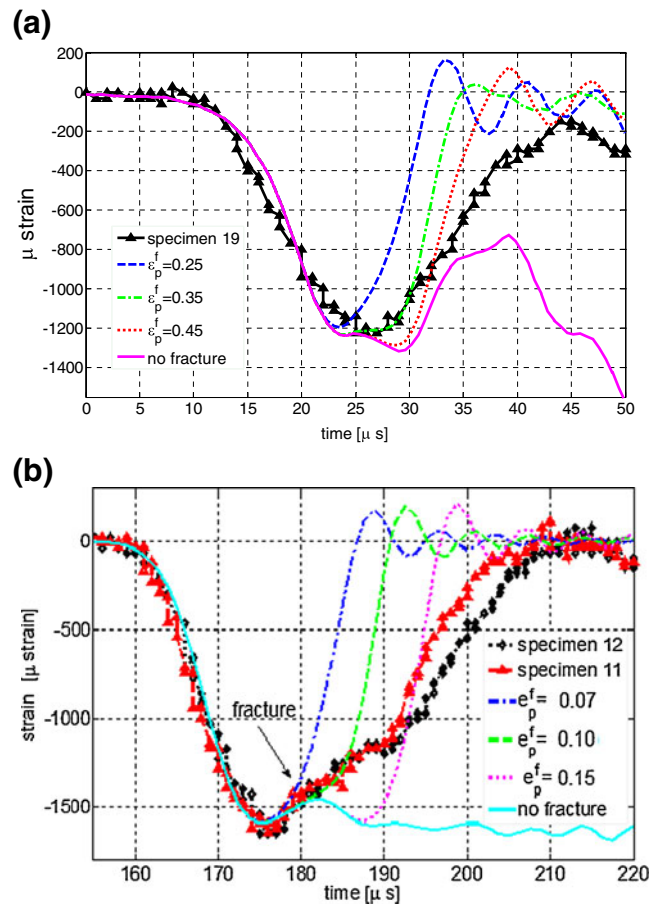


Fig. 8 Comparison of experimental transmitted strain to numerical calculated ones obtained for different fracture strains. (a). Specimen 19 of Table 1 showing that $\varepsilon_p^f = 0.35$. (b). Specimens 11 and 12 of Table 1 showing that $\varepsilon_p^f = 0.10$

of the transmitted bar (“transmitted strain”) for several values of fracture strain are shown in Fig. 8. It is assumed here that the correct fracture value is the one for which the simulated curve with fracture departs from the simulated curve without fracture at the strain for which the experimental curve departs from both.

Figure 8(a) shows the experimental transmitted strain of specimen 19 with the resultant numerical transmitted strain due to fracture strain of $\varepsilon_p^f = 0.25, 0.35, 0.45$ and no fracture. It should be noted that it is not expected from the numerical and the experimental signals to coincide beyond the fracture. The reason for that is that in experiments, the fractured surfaces remain in contact generating some frictional resistance, while in the numerical analysis this contact is not modeled. It can be observed that the simulation with $\varepsilon_p^f = 0.35$ agrees best with the time for departure between the experimental data and the no-fracture simulation. At that point, $t=26$ μ s, the distribution of the equivalent strain within the gauge is given in Fig. 9(a). The uniformity of the strain and its average value confirms the calculated fracture strain of $\varepsilon_p^f = 0.35$.

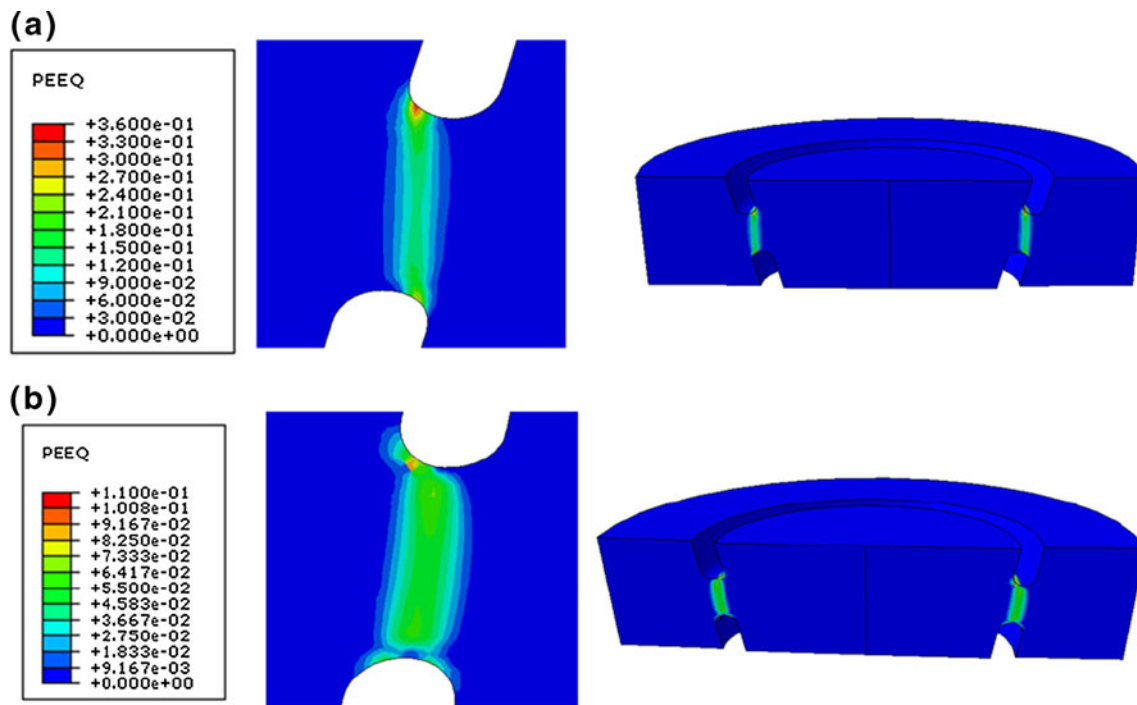


Fig. 9 Equivalent strain at the gauge at instant just prior to fracture for specimens 19 (a) and 12 (b)

Figure 8(b) shows the results for specimens 11 and 12. The point of fracture is estimated to be at $t=181 \mu\text{s}$. The best agreement for that point of fracture is obtained with $\varepsilon_p^f = 0.1$. The distribution of the equivalent strain within the gauge at that instant is shown in Fig. 9(b). The strain distribution is uniform and the average value is about 30 % lower than the fracture strain. The difference between the average value and the real fracture strain is related to stress (strain) concentration in the fillets.

The same procedure for the derivation of strain at fracture was repeated for each tested specimen. The results are summarized in Table 2, along with the average triaxiality in the gauge and the strain rate. The strain rate is obtained from the “converged” numerical solutions of the averaged stresses and plastic strain on the mid-line of the gauge. The triaxiality and strain rate are average values during loading. The triaxiality level within the gauge is approximately constant along the entire loading path up to fracture, and its distribution within the gauge is reasonably uniform (see details in [18]). This completes the process for derivation of the fracture strain for each experiment.

Discussion

A natural way to get a confidence in a particular experimental configuration designed for extraction of material properties is to compare the newly obtained properties with properties

acquired from already confirmed method. The first question to be addressed is whether the suggested specimen SCD is capable of reproducing the dynamic plastic flow within reasonable limits. To that end, additional experiments with two types of standard specimens, cylinder specimen (CS) and shear compression specimen (SCS), which are commonly used for dynamic stress–strain characterizations, were performed. Three CS and two cylindrical SCS [7] specimens were tested in a SHPB system. The cylinders had diameter of 6 mm and height of 6 mm. The SCS specimens had a diameter of 10 mm and total height of 20 mm. Their gauge height was 2 mm and thickness of 2.4 mm.

The cylinders were impacted at 3 different velocities and two types of analyses were used to interpret the results. The first is the “standard procedure” in which the pulses are analyzed using 1D wave theory for obtaining the $\sigma - \varepsilon$ curve (as in Appendix A). The second is an iterative numerical-experimental hybrid procedure which is described above for the SCD specimen. Namely, the experimentally measured incident pulse was used as an input in the numerical simulation and the resulting output strain signal is compared to the experimental signal. Convergence of the two signals served as a criterion for the required stress–strain curve.

The experimental results obtained by using the “standard procedure” for the three cylinder experiments are given in Fig. 10 and appear to confirm to the stress–strain curve defined by $\sigma_y=553 \text{ MPa}$ in Fig. 7 (the strain hardening in these two figures is identical). The iterative method led to

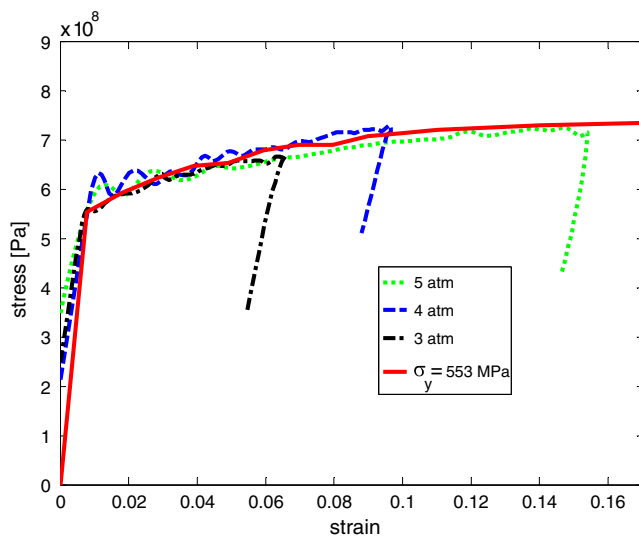


Fig. 10 Stress–strain curves of AL 7075-T651 at high strain rate (1000–3000 1/s) obtained from cylindrical specimens compared to an intermediate curve used to calculate the SCD specimens given in Fig. 7

identical result. Comparison of the numerically calculated transmitted pulses to the actual experimental pulse is shown in Fig. 11(a). The best agreement between the numerical simulation and the experimental result is obtained for a curve characterized by $\sigma_y = 553$ MPa. A similar value for the yield stress of that material is reported in [16]. That result provides some confidence in the iterative technique for stress–strain determination, although with some underestimation of the flow stresses by approximately 50 MPa as compared to the results obtained with SCD specimen.

The iterative procedure is further used to interpret the results from SCS specimens. The smoothed transmitted pulses of the SCS are shown in Fig. 11(b). It can be observed that the best agreement between the simulation and the numerical results is obtained again for a stress–strain curve defined by $\sigma_y = 553$ MPa. This agreement between the cylinder specimen and SCS specimen is notable. Yet, both differ from the result obtained using SCD specimen by 50 MPa.

A question can be raised on whether this discrepancy should cast a doubt on the validity of the SCD specimen for extraction of flow properties. Close comparison between the specimens and experiments disclose several differences which together could contribute to that deviation. The differences include: different material stock, different direction of main loading together with plastic anisotropy (e.g., [16, 27]), and different strain rate, especially, the non-constant strain rate in cylinder and SCS specimens. Moreover, even for quasi-static loading, a considerable difference between stress–strain curves obtained in tension and shear can be observed (as mentioned, e.g., [28–30]). For these reasons it turns out (a-posteriori) that the selected material is perhaps not an ideal choice for the calibration of the method suggested here. Yet, the elevation of 20% of the stress–strain

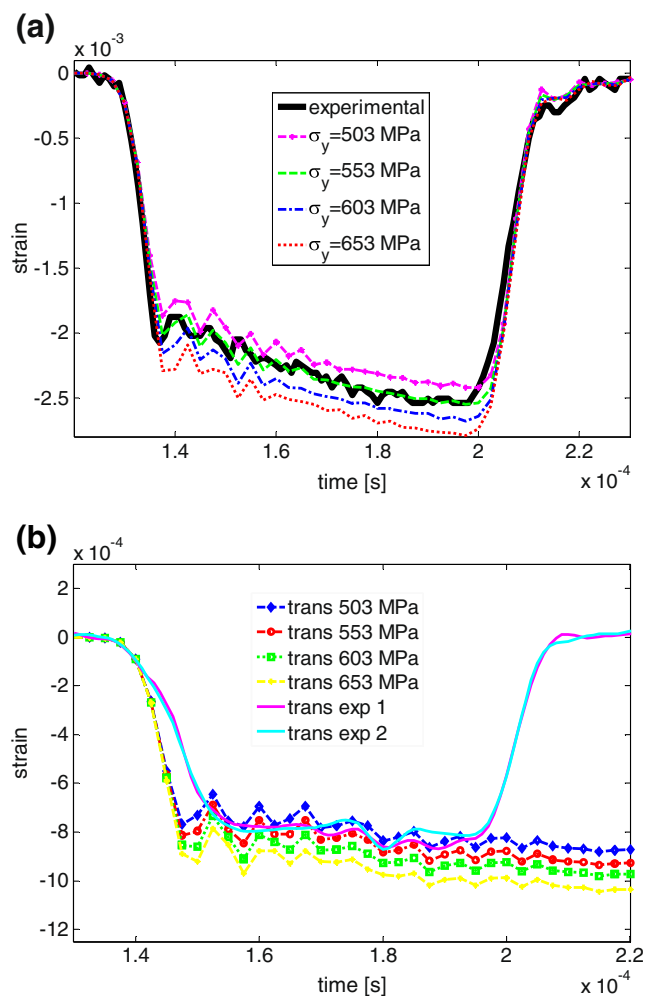


Fig. 11 comparison of the numerical transmitted pulses of the SHPB due to usage of 4 different $\sigma - \varepsilon$ curves of Fig. 7 to the actual experimental transmitted pulse. (a). Cylindrical specimen. (b). SCS specimens

curve due to rate effect obtained from SCD specimen, is consistent with the same elevation obtained in [31] for aluminum 7076-T6 using tension specimens. Therefore, it is concluded here that the SCD specimen is a valid candidate for material characterization, though additional work is required to further determine its accuracy.

The second issue to be discussed is whether the suggested SCD specimen is capable of characterizing a correct fracture strain, at any given triaxiality level and strain rate, within a reasonable limits. From procedural point of view, the correctness of the fracture strain obtained depends on the validity of the statement that the deviation of the experimental curve from the numerically simulated is rooted in fracture process, not simulated in first iteration simulations. Thereafter, the accuracy of the fracture strain determined by this procedure depends on a proper identification of the deviation point in Fig. 8 obtained from subsequent simulations. As a rough estimation of correctness of these

assumptions, let us compare the values for strain at fracture obtained by that procedure, to other independent results for that material.

A literature search for fracture data of 7075 aluminum alloy revealed reports only for tensile specimens where triaxiality is above 1/3 (necking increases triaxiality). The fracture strain reported is 0.28 [32] (for somewhat different heat treatment), $0.24 \div 0.28$ [33], and $0.17 \div 0.45$ [16]. Before one compares the results obtained here to these values, the large scatter in the results, possibly due to anisotropy as shown in [16], should be recognized. Moreover, even if there were no anisotropy at all, these results, obtained with tensile specimens, are still not free of assumptions. For example, calculation of fracture strain in tension specimens relies on Bridgman's assumption of uniform strain in the fractured cross-section [1], while it is known that it is not exact [13]. This leaves us with only a rough comparison (pointing again to a non-optimal choice of the material for such a benchmarking).

In order to compare our results obtained at low triaxiality levels we refer to [17], where it was shown that the fracture strain of aluminum 2024 at a triaxiality of -0.2 is approximately the same as at triaxiality of 1/3. Assuming similar behavior of these two aluminum alloys, one would expect same values at these triaxialities for aluminum 7075. Indeed, fracture strain obtained here for $tr = -0.2$ is 0.2, well within the scatter of the results in the literature for $tr = 1/3$.

In some aspects a more reliable confirmation for the procedure to obtain fracture from dynamic experiments is the comparison to fracture strain obtained under quasi-static conditions with the same specimen [18] where fracture strain was obtained by a completely different procedure. The fracture strains under quasi-static and dynamic condition for various levels of triaxiality are gathered in Fig. 12. It

can be observed that the fracture strain is of the same order of magnitude as in the static case and at $tr = 1/3$, giving some confidence in the procedure described in Section 5.2 for dynamic fracture.

Based on considerations given above it is suggested that the SCD specimen has beneficial properties making it suitable for the characterization of plasticity and fracture properties of metals. We proceed now to examine the possibility to identify from the experiments an approximate effect of triaxiality of stress and strain rate on the fracture strain.

Let us assume the mathematical dependence of fracture strain on triaxiality and strain rate can be expressed by the following relation

$$\varepsilon_p^f(t_r, \dot{\varepsilon}) = (c_1 + c_2 e^{c_3 t_r})(d_1 + d_2 \log(\frac{\dot{\varepsilon}}{\dot{\varepsilon}_r})) \quad (1)$$

which is a generalization of the Johnson-Cook failure model [34]. The two constants (d_1, d_2) are to be determined experimentally. The coefficients c_1, c_2 and c_3 are rate-independent and reported in [18] and $\dot{\varepsilon}_r$ is a reference strain rate which was taken here to be $\dot{\varepsilon}_r = 1$ [1/s]. A least squares technique is applied for fitting d_1 and d_2 to the experimental results detailed in Table 2. The difference between each experimental value $\varepsilon_p^f(i)$ to the value approximated by (equation (1)) is:

$$dif(i) = \varepsilon_p^f(i) - (c_1 + c_2 e^{c_3 t_r(i)})(d_1 + d_2 \log \dot{\varepsilon}(i)) \quad (2)$$

We minimize the sum of the squares of these differences:

$$F = \sum_{i=1}^{10} [dif(i)]^2 \quad (3)$$

by application of the partial derivatives

$$\frac{\partial F}{\partial d_1} = 0 ; \quad \frac{\partial F}{\partial d_2} = 0 \quad (4)$$

The solution of these two (equation (4)) yields: $d_1 = 0.8398$, $d_2 = -0.0173$. The value of the “dynamic term” $D^* = d_1 + d_2 \log \dot{\varepsilon}$, in (equation (1)) becomes $0.9991 \leq D^* \leq 1.0390$ for $1 \times 10^{-5} \leq \dot{\varepsilon} \leq 1 \times 10^{-4}$ [1/s] which means that (equation (1)) reduces to the quasi-static formula for quasi-static loading rates.

Figure 12 shows the experimental results of Table 2 as circles. The triangles stand for approximation of (equation (1)) to the values of Table 2. A good agreement is observed especially for the quasi-static experimental results. Three curves, obtained from (equation (1)) calculated for three values of strain rates: 0.0001, 1 and 10,000 [1/s], are shown in Fig. 12 as well. These curves show the prediction of (equation (1)) for the span of the fracture strain due to low, medium and high strain rate. Additional experimental results are needed for validating this material characterization.

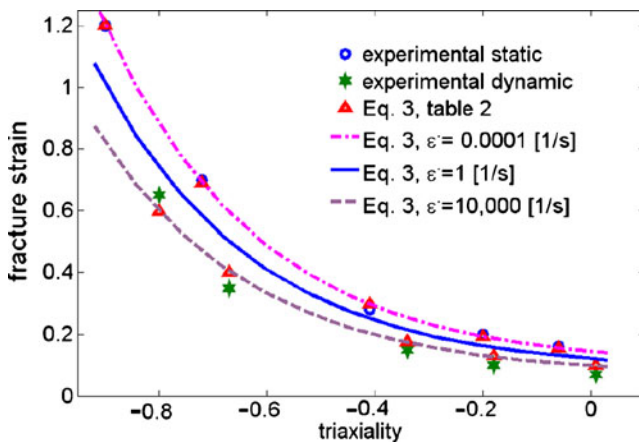


Fig. 12 The experimental fracture strain of Table 2 for aluminum 7075-T651 versus triaxiality. Experimental data, calculated values from (equation (1)), and best fit curves for (equation (1)) for 0.0001, 1 and 10000 [1/s]

Summary

The potential of the Shear Compression Disk specimen for characterization of high strain-rate flow and fracture properties of metals under various levels of triaxiality has been investigated. The main characteristics of that specimen, such as uniformity of stress within the gauge section and strain rate and triaxiality along the loading path, which were demonstrated for quasi-static loading [18], appear to hold for high strain rate loading as well. Specimens made of aluminum 7075-T651 were examined under various levels of stress triaxiality in a range of $0 < t_r < -0.8$ and the strain rate in the range of $3,000 < \dot{\varepsilon} < 15,000$ 1/s. Derivation of the plastic and fracture properties is based on a hybrid experimental - numerical method. The results for stress-strain curve were compared to cylinder and SCS specimen, showing reasonable agreement. Fracture strain was obtained for various levels for triaxiality and strain rates, emphasizing the advantage of the suggested specimen for a wide range of parameters (triaxiality and strain rate) with the same set of assumptions. Further experimental and numerical study is planned to extend our understanding on the benefits and the limitations of the SCD specimen.

Acknowledgement Financial support from Vatat (2013152) is greatly acknowledged. The authors wish to thank A. Amon and A. Reuven (Materials Mechanics Center) for their dedicated technical assistance.

Appendix A: A Method for Constitutive Relation Extraction

As an additional confirmation of the obtained stress-strain curve for the high strain-rate loading, the experimental results were interpreted directly using a similar procedure to the one which is applied for SCS specimens impacted in a SHPB apparatus. The procedure requires a transformation of the axial force and displacements on the SCD faces to the averaged von Mises stress and averaged total strain of the working line of the gauge (Fig. 3(a)). The procedure and its results are detailed here.

For that transformation the following derivation and relations have been used. We first verify numerically that, during impact the averaged Mises stress and the averaged total equivalent strain along the midline of the gauge (Fig. 3(a)), represent the $\sigma - \varepsilon$ curve which was inputted into the numerical simulation as the material property. This is similar to what has been shown for the shear compression specimen (SCS) [8] at strain rate of 3,000 1/s. Hence a similar data reduction technique can be used here for the shear compression disk (SCD). The

averaged total equivalent strain ($\hat{\varepsilon}$) on the mid-line of the gauge is related to the applied displacements (d) on the upper face of the specimen during the impact in the SHPB according to the approximate relation

$$\hat{\varepsilon}(t) = c_1 \frac{d(t)}{w} + c_2 \left(\frac{d(t)}{w} \right)^2 + c_3 \left(\frac{d(t)}{w} \right)^3 \quad (A1)$$

where w is the width of the slot. The averaged von Mises stress ($\hat{\sigma}$) on the mid-line of the gauge is related to the applied force (P) by:

$$\hat{\sigma}(t) = \left[c_4 \frac{P(t)}{\sigma_y A^s} + c_5 \left(\frac{P(t)}{\sigma_y A^s} \right)^2 + c_6 \left(\frac{P(t)}{\sigma_y A^s} \right)^3 \right] \sigma_y \quad (A2)$$

The applied force $P(t)$ is related to the measured transmitted strain $\varepsilon(t)$ by: $P(t) = \varepsilon_t(t) E A$ where E and A are elastic modulus and cross sectional area of the transmitting bar respectively. The sheared area of the gauge can be estimated by $A^s \cong Lh$ where L is the circumferential line: $L = \pi(D + w)$ where D is the inner diameter of the specimen's slots (equal to the incident bar diameter) and h is the vertical height of the specimen gauge. An average shear stress in the gauge is $P(t)/A^s$. Equation (A2) simply approximates the normalized von Mises stress on the mid-line of the gauge $\hat{\sigma}(t)/\sigma_y$ to the normalized averaged applied shear $\frac{P(t)}{\sigma_y A^s}$ where the static yield stress of the specimen is σ_y . The coefficients c_i , $i = 1 \dots 6$ are calculated from the numerical analysis. Using for example the known static properties of Aluminum 7075-T651 and simulating the impact of a specimen with $\beta = 15^\circ$ (specimen 17 - Table 1) the

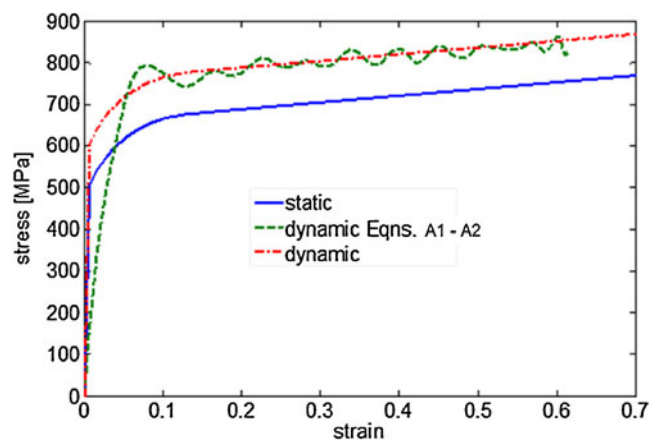


Fig. 13 Comparison of the quasi-static (blue) and dynamic (green, red) $\sigma - \varepsilon$ curves for Aluminum 7075-T651 obtained by specimen 17. The resulting dynamic experimental $\sigma - \varepsilon$ curve (green) is obtained by application of (equations (A1) and (A2)) with the experimental results ($d(t), P(t)$). The resultant dynamic $\sigma - \varepsilon$ curve (red) is numerical modification of the green line

coefficients are: $c_1=0.14442$, $c_2=0.81074$, $c_3=-0.40775$, $c_4=3.6816$, $c_5=-4.4228$ and $c_6=2.4896$. Using (Equations (A1) and (A2)) with these coefficients and the experimentally measured ($d(t)$, $P(t)$) yield the first approximation for the dynamic $\sigma - \varepsilon$ curve. The resulting stress–strain curve is shown here in Fig. 13 along with the quasi-static curve and the dynamic curve obtained by the iterative process employing full numerical simulation (Fig. 7). An agreement in the results obtained by the two analyses is noted.

References

1. Bridgman PW (1952) Studies in Large Plastic Flow. McGraw-Hill
2. Rice JR, Tracey DM (1969) On the ductile enlargement of voids in triaxial stress fields. *J Mech Phys Solids* 17:201–217
3. Ramesh KT (2002) Effects of high rates of loading on the deformation behavior and failure mechanisms of hexagonal close-packed metals and alloys. *Metall Mater Trans A* 33A:927–935
4. Edwards M (2006) Properties of metals at high rates of strain. *Mater Sci Tech* 22:453–462
5. Meyers MA, Xu YB, Xue Q, Pérez-Prado MT, McNeley TR (2003) Microstructural evolution in adiabatic shear localization in stainless steel. *Acta Mater* 51:1307–1325
6. Kad BK, Gebert JM, Perez-Prado MT, Kassner ME, Meyers MA (2006) Ultrafine-grain-sized zirconium by dynamic deformation. *Acta Mater* 54:4111–4127
7. Rittel D, Ravichandran G, Lee S (2002) A shear compression specimen for large strain testing. *Exp Mec* 42:58–64
8. Ames M, Markmann J, Birringer R (2010) Mechanical testing via dominant shear deformation of small-sized specimen. *Mat Sci Eng A-Struct* 528:526–532
9. Masson I, Guegan P, Lesaffre AS, Quirion Y, Poitou A (2006) Dynamic compressive testing under confining pressure on a quasi-brittle material. *J Phys Iv* 134:707–712
10. Rittel D, Hanina E, Ravichandran G (2008) A note on the direct determination of the confining pressure of cylindrical specimens. *Exp Mech* 48:375–377
11. Mae H, Teng X, Bai Y, Wierzbicki T (2008) Comparison of ductile fracture properties of aluminum castings: Sand mold vs. metal mold. *Int J Solids Struct* 45:1430–1444
12. Mae H (2009) Characterization of material ductility of PP/EPR/talc blend under wide range of stress triaxiality at intermediate and high strain rates. *Journal of Applied Polymer Science* 111:854–868
13. Alves M, Jones N (1999) Influence of hydrostatic stress on failure of axisymmetric notched specimens. *J Mech Phys Solids* 47:643–667
14. Barton DC (2004) Determination of the high strain rate fracture properties of ductile materials using a combined experimental/numerical approach. *Int J Impact Eng* 30:1147–1159
15. Børvik T, Hopperstad OS, Dey S, Pizzinato EV, Langseth M, Albertini C (2005) Strength and ductility of Weldox 460 E steel at high strain rates elevated temperatures and various stress triaxialities. *Eng Fract Mech* 72:1071–1087
16. Børvik T, Hopperstad OS, Pedersen KO (2010) Quasi-brittle fracture during structural impact of AA7075-T651 aluminium plates. *Int J Impact Eng* 37:537–551
17. Wierzbicki T, Bao Y, Lee Y-W, Bai Y (2005) Calibration and evaluation of seven fracture models. *Int J Mech Sci* 47:719–743
18. Dorogoy A, Karp B, Rittel D (2011) A shear compression disk specimen with controlled stress triaxiality under quasi-static loading. *Exp Mech* 51:1545–1557
19. Abaqus/CAE version 6.9-EF1 2009. Dassault Systemes Simulia Corporation, Providence, RI, USA
20. Klepaczko JR (1994) An experimental technique for shear testing at high and very high strain rates. the case of a mild steel. *Int J Impact Eng* 15:25–39
21. Roessig KM, Mason JJ (1999) Adiabatic shear localization in the dynamic punch test, part I: experimental investigation. *Int J Plasticity* 15:241–262
22. Rusinek A, Klepaczko JR (2001) Shear testing of a sheet steel at wide range of strain rates and a constitutive relation with strain-rate and temperature dependence of the flow stress. *Int J Plasticity* 17:87–115
23. Li QM, Jones N (2002) Response and failure of a double-shear beam subjected to mass impact. *Int J Solids Struct* 39:1919–1947
24. Li Z, Bi X, Lambros J, Geubelle PH (2002) Dynamic fiber debonding and frictional push-out in model composite systems: experimental observations. *Exp Mech* 42:417–425
25. Dabboussi W, Nemes JA (2005) Modeling of ductile fracture using the dynamic punch test. *Int J Mech Sci* 47:1282–1299
26. Abaqus/CAE version 6.9-EF1 (2009) Abaqus documentation. Abaqus Analysis User's Manual, chapters 20–21, Dassault systemes. Springer, New York
27. Pedersen KO, Børvik T, Hopperstad OS (2011) Fracture mechanisms of aluminium alloy AA7075-T651 under various loading conditions. *Materials and Design* 32:97–107
28. Rauch GC, Leslie WC (1972) The extent and nature of the strength-differential effect in steels. *Metall Trans* 3:373–385
29. Mahnen R (2001) Strength difference in compression and tension and pressure dependence of yielding in elasto-plasticity. *Comput Method Appl M* 190:5057–5080
30. Gao X, Zhang T, Hayden M, Roe C (2009) Effects of the stress state on plasticity and ductile failure of an aluminum 5083 alloy. *International Journal of Plasticity* 25:2366–2382
31. Nicholas T (1981) Tensile testing of materials at high rates of strain. *Experimental Mechanics* 21:177–185
32. Celentano DJ, Cabezas EE, Garcia CM, Monsalve AE (2004) Characterization of mechanical behaviour of materials in the tensile test: experiments and simulation. *Modelling Simul Mater Sci Eng* 12:S425–S444
33. Brar NS, Joshi VS, Harris BW (2009) Constitutive model constants for Al7075-T651 and Al7075-T6. Shock Compression of Condensed Matter – 2009, Eds. Elert ML, Buttler WT, Anderson WW, Proud WG. American Institute of Physics
34. Johnson GR, Cook WH (1985) Fracture characteristics of three metals subjected to various strains, strain rates, temperatures and pressures. *Engineering Fracture Mechanics* 21:31–48